Flame-vortex interactions - Effects of buoyancy from microgragity imaging studies

J. O. Sinibaldi
Michigan Univ., Ann Arbor

J. F. Driscoll
Michigan Univ., Ann Arbor

C. J. Mueller
Michigan Univ., Ann Arbor

A. E. Tulkki
Michigan Univ., Ann Arbor

AIAA, Aerospace Sciences Meeting & Exhibit, 35th, Reno, NV, Jan. 6-9, 1997

The interaction between a single toroidal vortex and a laminar flame in a lean premixed propane-air mixture was visualized in order to understand how each vortex in a turbulent flow wrinkles, stretches, and possibly extinguishes the flame. Both microgravity and 1-g images were obtained to identify the role of buoyancy forces, which are significant in laboratory flames and in many industrial flames. Buoyancy forces affect the degree of flame wrinkling, the vorticity produced by the flame due to baroclinic torques, the flame stability, and the flame velocity. In the present experiment, all components of flame stretch, strain, and vorticity can be measured from a single PIV image because the interaction is axisymetric. Results indicate that microgravity conditions greatly augment the flame wrinkling process and therefore turbulent flames in microgravity could propagate significantly faster than those in 1-g, which is a potential safety hazard. A new mechanism is identified by which buoyancy retards flame wrinkling; buoyancy produces new vorticity (due to baroclinic torques) that oppose the wrinkling and stretch imposed by the original vortex. (Author)

FLAME - VORTEX INTERACTIONS: EFFECTS OF BUOYANCY FROM MICROGRAVITY IMAGING STUDIES

J. O. SINIBALDI*, J. F. DRISCOLL†, C. J. MUELLER‡, and A. E. TULKKI§

Department of Aerospace Engineering, The University of Michigan, Ann Arbor, MI 48109

The interaction between a single toroidal vortex and a laminar flame in a lean premixed propane-air mixture was visualized in order to understand how each vortex in a turbulent flow wrinkles, stretches, and possibly extinguishes the flame. Both microgravity and one-g images were obtained to identify the role of buoyancy forces, which are significant in laboratory flames and in many industrial flames. Buoyancy forces affect the degree of flame wrinkling, the vorticity produced by the flame due to baroclinic torques, the flame stability and the flame velocity. In the present experiment, all components of flame stretch, strain, and vorticity can be measured from a single PIV image because the interaction is axisymetric. Results indicate that microgravity conditions greatly augment the flame wrinkling process and therefore turbulent flames in microgravity could propagate significantly faster than those in one-g, which is a potential safety hazard. A new mechanism is identified by which buoyancy retards flame wrinkling; buoyancy produces new vorticity (due to baroclinic torques) that oppose the wrinkling and stretch imposed by the original vortex. Microgravity conditions remove this stabilizing mechanism and the amplitude of flame wrinkling is found to increase by a factor of 3 to 4. The flame speed is also increased by a factor of 1.8 to 2.2. Hence, these results indicate that it is important to add buoyancy terms to models of turbulent flames in order to simulate the correct degree of flame wrinkling, stretch and burning velocity.

INTRODUCTION

In recent years, research in the area of turbulent combustion has focused on two important mechanisms that previously were not understood: the effects of stretch/preferential diffusion, and the effects of buoyancy forces. It is not surprising that previous efforts that ignored these mechanisms and yet attempted to measure or numerically predict fundamental quantities (such as the turbulent burning velocity) have yielded results that display a large amount of scatter and uncertainty. For example, buoyancy is important in many of the laboratory flames from which our knowledge of turbulent combustion is derived. Buoyancy can affect turbulent Bunsen flames [1]. V - flames, counterflow turbulent flames, and spherical turbulent flames [2], making it difficult to compare the results of different studies.

It is well known that buoyancy affects the velocity of a flame in a tube; flames propagate upward at a higher velocity than they propagate downward [3]. Several reasons for this difference have been proposed: hot gases underneath an upward propagating flame act as a hot bubble that rises due to buoyant forces. Conversely, the hot gases above the downward propagating flame accelerate away from the reaction zone and this additional convection of heat away from the reaction zone tends to slow the reactions. Buoyancy forces may set up a recirculatory motion of the reactants [3].

In a typical turbulent flame the hot products are above the cold reactants and as each vortex wrinkles the flame, buoyancy forces can (a) reduce flame wrinkling by opposing the fluid forces that would lift heavy pockets of cold reactants ("the stabilizing effect of buoyancy"), (b) reduce flame wrinkling by creating "flame generated vorticity" that opposes the motions induced by vortices, as shown below, and (c) increase the upward velocity of

the products away from the reaction zone ("the chimney effect") which is an additional convective heat loss that reduces the reaction rate and velocity of a downward-propagating flame. Therefore microgravity flames can have a larger amplitude of flame wrinkling and a larger velocity because the inhibiting effects of buoyancy have been removed, as shown below.

One reason for measuring flame wrinkling and stretch is the need to model the flame stretch terms that appear in the new models of turbulent combustion. Flame surface density models now are used extensively in the automotive and gas turbine industry and rely on the conservation equation for flame surface density, Σ:

$$\frac{D\Sigma}{Dt} = K_m \Sigma - D + \frac{\partial}{\partial x_i}\left(v_i \frac{\partial \Sigma}{\partial x_i}\right) \qquad (1)$$

The rate at which flame surface density of a turbulent flame changes in time ($D\Sigma/Dt$) depends on the rate of production of surface density ($K_m\Sigma$) which is proportional to the mean stretch rate K_m. Measurements of the instantaneous stretch rate such as those described below, are needed to properly model the mean stretch rate. The last two terms in Eq. 1 quantify the rates of the destruction (D) and diffusion of flame surface density.

The goals of the present work are: to quantify the effects of buoyancy and visualize the relevant physics, and to provide benchmark data that is buoyancy-free which can be used to assess Direct Numerical Simulations of flame-vortex interactions and to improve turbulent combustion models. The present flame-vortex interaction experiment has been used at one-g by Driscoll, et al. [4] and Mueller, et al. [5] to measure the local stretch rate of a wrinkle flame; images of OH concentrations and the flame wrinkling process were reported by Mueller, et al. [6, 7], and Roberts, et al. [8-10].

EXPERIMENTAL ARRANGEMENT

Microgravity Drop Tower Experiment

The experiment that was dropped at the NASA Lewis 2.2 Second Drop Tower is shown in Fig. 1a, while Fig. 1b shows the layout of the drop package and Fig. 1c illustrates the power/control circuits on the drop package. The combustion chamber is similar to a previous design described in Refs. 4-9. A central rectangular chamber is filled with a lean propane-air mixture at equivalence ratio of 0.55. Two spark electrodes are mounted near the top of the chamber which ignite the mixture on the centerline. A laminar flame propagates downward; the typical flame

speed is 10 cm/s at one-g and 20 cm/s at zero-g. At the bottom of the chamber a loudspeaker is mounted 3 cm below a metal plate having a 2.5 cm diameter orifice. Pulsing the loudspeaker forces fluid through the orifice, forming a laminar toroidal vortex ring that moves upward and interacts with the flame. The vortex strength is controlled by adjusting the maximum voltage applied to the loudspeaker; vortex strength is defined as the maximum rotational velocity (which occurs at the edge of the vortex core [9]); it varies from 10 to 100 cm/s. The propane-air mixture inside the vortex is identical to that of the chamber into which the vortex moves. The microgravity flame is visualized using two methods: a video camera records the direct flame emission, and on other runs oil drops or silicon solid particles are introduced and are illuminated by a white light sheet. The white light sheet is formed using a pulsed Xenon arc lamp that provides 0.5 joule pulses at 60 pulses/sec with a 10 microsecond pulse duration that is short enough to freeze the fluid motion. Each half-frame of the video camera is synchronized with the light source, so images are obtained at a 60 Hz rate. For one-g runs, PIV and OH LIF diagnostics have been used [4 - 9].

Three vortex strengths were used, corresponding to the regimes of: wrinkled thin flames, corregated flames having pockets of unreacted gas, and local flame extinction.

PIV Velocity Field Imaging System for One-g Tests

To date, PIV images have been obtained only for the one-g tests; future work will be directed toward obtaining corresponding PIV images in zero-g. The one-g images do, however, identify some effects of buoyancy since cases were run at three different values of the Froude number, Fr, defined as:

$$Fr = \frac{U_\theta^2}{g\,d} = 0.2, 1.6, 17 \qquad (2)$$

where U_θ is the maximum rotational velocity of the vortex which occurs near the vortex core, and d is the 0.77 cm core diameter. Buoyancy has a strong stabilizing effect at Fr = 0.2, whereas it does not at Fr = 17. However, buoyancy forces are not the only phenomena that change as conditions are changed to increase Fr from 0.2 to 17; the flame enters a different regime where flame extinction and chemistry also differ, so microgravity studies are essential to truly remove the effects of buoyancy. The one-g PIV measurements were made with exceptional spatial resolution of 0.5 mm between valid velocity vectors such that four velocity grid points fit within the 2 mm thick flamefront. Thus it is possible to focus on how

the gas velocity and flame stretch varies within the flame and along the flame front, even if it becomes highly wrinkled. Velocity derivatives were measured with sufficient resolution to deduce several important properties of the interaction, including (a) the decaying strength of the vortex (i.e. measured vorticity) as the vortex is destroyed by the flame, (b) the new "flame-generated" vorticity that is created by the flame, and (c) the strain rate and stretch exerted on the flame, which are needed in numerical simulations.

The PIV system is shown in Figs. 2a and 2b and is described in detail in Refs. 5, 6 and 11. It consists of two frequency-doubled YAG lasers operated in the green at 532 nm. Optics are used to produce two 100 mJ pulsed light sheets whose time separation can be varied from 0.05 to 0.35 ms and whose thickness is 200 microns. The first light sheet consists of vertically polarized light while the second sheet consists of horizontally polarized light. A birefringent calcite crystal was mounted in front of the lens of a 70 mm Toyo camera in order to spatially shift the images from the two laser sheets to eliminate directional ambiguity. Each photographic negative (70 mm Kodak Tech-Pan, 300 lines per mm) was scanned with a TSI Model 6000 PIV Analyzer, which interrogates each 1.25 mm x 1.25 mm spot. A second spot is identified that has the same dimensions but is located 0.5 mm away from the first spot and overlaps about 50% of the first spot. The cross correlation between the two spots is determined and its peak value identifies the velocity associated with the first spot. This method inherently captures many particles that have moved out of the first spot region and into the second spot region between the laser pulses, so it substantially increases the signal-to-noise over the standard autocorrelation method [10]. Typically there were about 20 particle pairs in each interrogation spot and 50 particles/mm^3.

Time resolution is achieved by running the highly repeatable experiment many times and acquiring one PIV image per run. Shadowgraph movies of the flame position and flame shape were taken at 1000 frames per second in order to accurately measure the time of interaction of a particular PIV image and to quantify the high degree of repeatability of the experiment.

Data Reduction

Video images of the microgravity flames were digitized using a frame grabber board and the gray scale of the black-and-white video images was converted to a color scale using Adobe Photoshop software on a Macintosh computer. The PIV images of the one-g flames typically had 94% of the 10,000 grid locations on each image filled with validated velocity vectors. The remaining 6% of the grid locations had no validated

velocity vectors because of index of refraction distortions caused by the flamefront and linear interpolation was used.

The instantaneous flame stretch rate, K, was determined using the definition [5]:

$$K = -\hat{n} \cdot (\hat{n} \cdot \nabla) \vec{u} + \nabla \cdot \vec{u} + \frac{S_L}{R} \qquad (3)$$

The first term is the strain rate due to gradients in the velocity that is normal to the flame, the second term accounts for the divergence of the velocity field, and the third term is due to the flame radius of curvature R. The divergence operator, ∇, is represented in cylindrical coordinates and thus all components of stretch are measured in this axisymetric experiment. Since the third term contributes less than 5% of the total stretch rate, S_L is approximated by its unstretched value. The form of Eq. 2 that was used to deduce stretch rate, K, was:

$$K = \frac{u_r}{r} + n_z^2 \frac{\partial u_r}{\partial r} - n_r n_z \left(\frac{\partial u_r}{\partial z} + \frac{\partial u_z}{\partial r} \right)$$
$$+ n_z^2 \frac{\partial u_z}{\partial z} + \frac{S_L^\circ}{R} \qquad (4)$$

The upstream boundary of the flame first was defined by using the measured values of u_r and u_z to determine $\nabla \vec{u}$ at each grid location (every 0.5 mm). The upstream flame boundary is defined as the following contour $\nabla \vec{u} = 0.25 \ (\nabla \vec{u})_{max}$ where $(\nabla \vec{u})_{max}$ is typically 400 s^{-1}. Along this upstream contour of the flame the normal vector, $\hat{n}$, and its components n_r and n_z were deduced. Derivatives such as $\partial u_r / \partial r$ were determined by fitting measured values of u_r at five grid locations in the r direction with a quadratic polynomial and then analytically computing the derivative at the central grid position. The radius of curvature, R, at each point on the (axisymetric) upstream boundary of the flame was computed using standard geometric formulas [12]. Two orthogonal planes were passed through the normal vector, $\hat{n}$, and the intersections of these planes define two curves which were fit with 10th order polynomials. The derivatives of these polynomials yield the two principal radii of curvature $(R_1$ and $R_2)$ and R equals:

$$R = \frac{1}{R_1} + \frac{1}{R_2} \qquad (5)$$

RESULTS

Amplitude of the Wrinkle in Microgravity Flames

Images of the flame-vortex interaction under microgravity conditions are shown on the right side of Figs. 3, 4 and 5. Three vortex strengths were chosen; Fig. 3 represents the "weak vortex" case, Fig. 4 represents the "intermediate strength vortex", and Fig. 5 represents the "strong vortex" case. For comparison, the left side of Figs. 3, 4, and 5 show the one-g flame images that were recorded immediately after each successful microgravity drop.

As shown in Fig. 3, the flame propagates downward and the vortex moves upward. It is seen that the amplitude of wrinkling is significantly larger in the microgravity cases (on the right) than in the corresponding one-g cases (on the left) in Figs. 3 - 5. This difference is partially due to the "stabilizing effect" of buoyancy forces at one-g; buoyancy acts against the vortex-induced forces which attempt to lift the heavier cold reactants. Buoyancy also creates new vortices at the flame interface, as shown below, which suppress the wrinkling seen in Figs. 3-5.

Figure 4 shows that under microgravity conditions, the intermediate strength vortex is more effective at thickening and distorting the flame. Small circular regions of more intense chemical reaction appear within the microgravity flames on the right side. The flame is severely thickened in microgravity, most likely because the strain forces exerted by the vortex are not counteracted by buoyant forces.

Figure 5 indicates that for the strongest vortex case, the microgravity flames also are more severely thickened and distorted than the one-g flames. The strong vortex case was selected because pockets of reactants are formed (as seen in Fig. 5) and thus the flame has moved into the "corregated flame" regime. In highly turbulent flows such as found in IC engines, corregated flames occur, having many isolated pockets of unburned reactants and other pockets of burned products.

The effect of microgravity on the amplitude of the flame wrinkling is plotted in Fig. 6. Each graph is a time history of the distance on centerline between the distorted flame position and the undistorted flame location. It is seen that for all three vortex strengths, microgravity causes the amplitude of wrinkling to be larger (as much as a factor of two larger) than that experienced at one-g.

Velocity Fields and Stretch Rates in One-G Flames

Figure 7 is a typical image of 6,000 velocity vectors that was recorded at one-g using the PIV system. The total field of view is larger than shown in Fig. 7 and consists of 10,000 vectors, but the edge region has been omitted for clarity. The toroidal vortex core appears as the two counter rotating regions at an axial coordinate value of 35 mm. The flame appears as the curved boundary where there is an abrupt change in the magnitude and direction of the vectors.

The real advantage of this type of experiment is demonstrated by Fig. 7. The vortex can be made large enough so that many velocity vectors along the flame can be recorded. The lean flame provides a large value of flame thickness of 2 mm, so the ratio of vortex diameter to flame thickness (d/δ_f) is in a realistic range, yet both dimensions are large enough so that gradients can be resolved along the flame. This is not possible in turbulent flames. Approximately 200 images, similar to Fig. 7, have been obtained at one-g for a wide range of vortex strengths and interaction times.

A time history of the flame-vortex interaction is shown for the three vortex strengths in Figs. 8, 9, and 10. For clarity, only every ninth velocity vector is plotted. While each image was obtained on a different run, the repeatability of the experiment is excellent so the images represent a time history. The right side of the figures shows the contours of the vorticity field, which is used to determine how the primary vortex is attenuated as it passes through the flame, and how new vortices can be created at the flame surface in some cases. It is important to know if small vortices are attenuated and thus do not wrinkle the flame because such vortices can be correctly neglected in Direct Numerical Simulations and Large Eddy Simulations of turbulent flames.

Figure 8 shows that the weak vortex is totally attenuated by the flame. However, in this low Froude number case (Fr = 0.2) buoyancy creates a new vortex in the products that actually is stronger (with larger values of vorticity and circulation) than the original vortex. The "flame-generated" vortex appears in Fig. 8 as the region above (downstream) of the flame; it is rotating in a direction that is opposite to the original vortex. The flame generated vortex is caused by baroclinic torques that arise near the flame surface [5].

A new mechanism has been identified which represents an additional way that buoyancy can stabilize a flame. Previously it has been known that buoyancy exerts a downward body force that oppose the upward motion of the more dense cold reactants. The additional mechanism is identified by the data in Fig. 8. The "flame generated vorticity" that is above the flame in Fig. 8 is due to buoyancy-induced baroclinic torques; this new vorticity imparts a rotational velocity that counteracts the velocity imparted by the primary vortex. For example, on centerline the initial vortex imparts an upward velocity that tends to exert extensional strain and increases the

4

flame wrinkling; the flame generated vortex that is caused by buoyancy imparts a downward velocity on centerline which reduces the wrinkling and stretch.

For the intermediate strength vortex, the PIV images in Fig. 9 show that some of the vortex survives the flame passage, unlike the weak vortex case. Some "flame generated vorticity" also is created so that in the final image there are two separate toroidal vortices having opposite vorticity. The strong vortex shown in Fig. 10 survives flame passage without being attenuated and does not create any "flame generated vorticity." The strong vortex locally extinguishes the flame, so the flame enters a new regime of combustion, denoted the thick flamelet regime in which reactants and products can coexist for a short period of time. A more thorough discussion of the vorticity attenuation and generation by this flame is found in Ref. 5.

Two important parameters are the local stretch rate (K), which was determined using Eq. 3, and the local velocity divergence ($\nabla \bar{u}$) which is an indicator of the overall heat release rate due to chemical reaction [6]. The PIV data is sufficiently resolved to determine these quantities for the first time for a freely propagating flame. Figure 11 shows that for the strongest vortex, the stretch rate is 200 s^{-1} on centerline but rapidly drops to -200 s^{-1} near the neck of the wrinkled flame. For this lean propane-air reaction, the Markstein number is eight and theory predicts that the chemical reaction will be suppressed near the centerline and will be enhanced near the neck region where the stretch is negative. The measurements in Fig. 11 show that the theory is correct. The upper curve labeled Δ is the peak value of the velocity divergence which is an indicator of the chemical heat release rate. This curve has a maximum where the stretch rate is negative, as is predicted by theory. Similarly, Fig. 12 shows that at a later time the location of negative stretch corresponds to a maximum of the heat release rate, as quantified by the curve denoted Δ. The flame begins to show evidence of extinction in Fig. 12 and later significant extinction is seen in Fig. 13. Extinction is identified by regions along the continuous flamefront where $\nabla \bar{u}$ drops nearly to zero.

It also is concluded that the flame does not respond immediately to the imposed stretch rate, but that unsteady effects occur. The stretch rate on centerline is quantified in Fig. 11 to be 220 s^{-1}, which is five times larger than the stretch rate of 42 s^{-1} that extinguishes a steady state counterflow flame in a lean propane-air mixture at an equivalence ratio of $\phi = 0.55$. The flame does not immediately extinguish but requires approximately 21 ms for extinction to begin. The characteristic chemical time for the flame is the thickness of the OH layer (0.15 cm) divided by the flame speed (10 cm/s); this time is 15 ms. Thus the extinction does not begin until 1.5 chemical times have elapsed. This indicates that unsteady effects are important and that the flame cannot be modeled as an interface that responds immediately to the imposed stretch rate, as has been proposed. Instead unsteady flame simulations [13] are believed to most accurately represent the present flame properties.

CONCLUSIONS

The amplitude of the wrinkle in the flame caused by a single vortex is 1.5 to 2 times larger under microgravity conditions than in the corresponding one-g case, for the same vortex strength.

The laminar flame speed S_L for the lean propane-air mixture in the microgravity case is 1.8 to 2.2 times larger than that of a flame moving downward at one-g. This is consistent with previous observations that buoyancy causes flames that move upward within tubes to move faster than those that propagate downward.

Proper comparison requires that both the microgravity and one-g results be compared for the same ratio of vortex strength to laminar burning velocity, that is U_θ / S_L. When this proper parameter is used, the microgravity flames have approximately three to four times the amplitude of wrinkling of that of the one-g flames, for the same value of U_θ / S_L. This is a significant difference and it suggests that microgravity turbulent flames will wrinkle and propagate significantly faster, and may pose more of a safety hazard, than corresponding one-g flames.

The one-g PIV work provided images of a new physical mechanism that explains why the flames become significantly more wrinkled in microgravity. PIV images show that new vorticity is created by buoyancy which suppresses the wrinkling at one-g. When this mechanism is removed in microgravity, the flames wrinkle more freely. Adding this mechanism would make models of turbulent combustion more realistic.

Flames in microgravity are more curved than at one-g because buoyancy forces flatten the present one-g flame.

The microgravity flames appear to have a thicker reaction zone than the one-g flames, but further work is required to see if this is real or an artifact of the experiment. The microgravity flames have a higher velocity so that blurring due to the camera shutter speed may be larger in the microgravity case.

The present experiment provides flames that are stable and wrinkle-free prior to the vortex interaction. The synchronization techniques that are required to overlap the flame, vortex and light sheet at the correct time during the microgravity drop tests were successful and highly repeatable.

American Institute of Aeronautics and Astronautics

ACKNOWLEDGMENT

REFERENCES

1. Wu, M.S., Kwon, S., Driscoll, J.F., and Faeth, G.M., Combust. Sci. Technol. 73, pp. 327-350, 1990.

2. Abdel-Gayed, R., Bradley, D., Hamid, M. and Lawes, M., Twentieth Symposium (International) on Combustion, The Combustion Institute, 1984, p. 505.

3. Lewis , B. and von Elbe, G., Combustion, Flames and Explosions of Gases, Academic Press, New York, 1961.

4. Driscoll, J.F., Sutkus, D., Roberts, W., Post, M. and Goss, L. "The Strain Exerted by a Vortex on a Flame - Determined From Velocity Field Images", Combustion Science and Technology, 96, 213-229, 1994.

5. Mueller, C. J., Driscoll, J.F., Reuss, D., Drake, M., "Generation and Attenuation of Vorticity by Flames: Measured Vorticity Field Time Evolution", to appear, Combustion and Flame.

6. Mueller, C., Driscoll, J. F., Reuss, D. and Drake, M. "Effect of Unsteady Stretch on the Strength of a Freely Propagating Flame Wrinkled by a Vortex", to appear, Proceedings of the Twenty-Sixth Symposium (International) on Combustion, Naples

7. Mueller, C., Driscoll, J.F., Roberts, W.L., Drake, M.C., and Smooke, M.D., "Effect of Stretch Rate on Flame Chemistry During a Transient Flame-Vortex Interaction - to Assess Flamelet Models", Twenty-Fifth Symposium (International) on Combustion, published in Combustion and Flame 100, 323-331, 1995.

8. Roberts, W. and Driscoll, J.F. "A Laminar Vortex Interacting With a Premixed Flame: Formation of Pockets of Reactants", Combustion and Flame 87:245-256, 1991.

9. Roberts, W.L., Driscoll, J.F., Drake, M.C. and Ratcliffe, J. "OH Fluorescence Images of the Quenching of a Premixed Flame by a Vortex", Twenty-Fourth Symposium (International) on Combustion, pp. 169-176, Sydney Australia, (1992).

10. Roberts, W.L., Driscoll, J. F., Drake, M.C. and Goss, L.P. "Images of the Quenching of a Flame By a Vortex - To Quantify Regimes of Turbulent Combustion", Combustion and Flame 94:58-69, 1993.

11. Reuss, D.L., Bardsley, M., Felton, P., Landreth, C., and Adrian, R., SAE Paper 900053, 1990.

12. Lipshutz, M.M., Theory and Problems of Differential Geometry, McGraw-Hill, N.Y. p. 171, 1969.

13. Wu, M.S. and Driscoll, J. F. "Simulations of a Premixed Flame-Vortex Interaction Using a SLIC Interface Algorithm", Combustion and Flame 91:310-322, 1992.
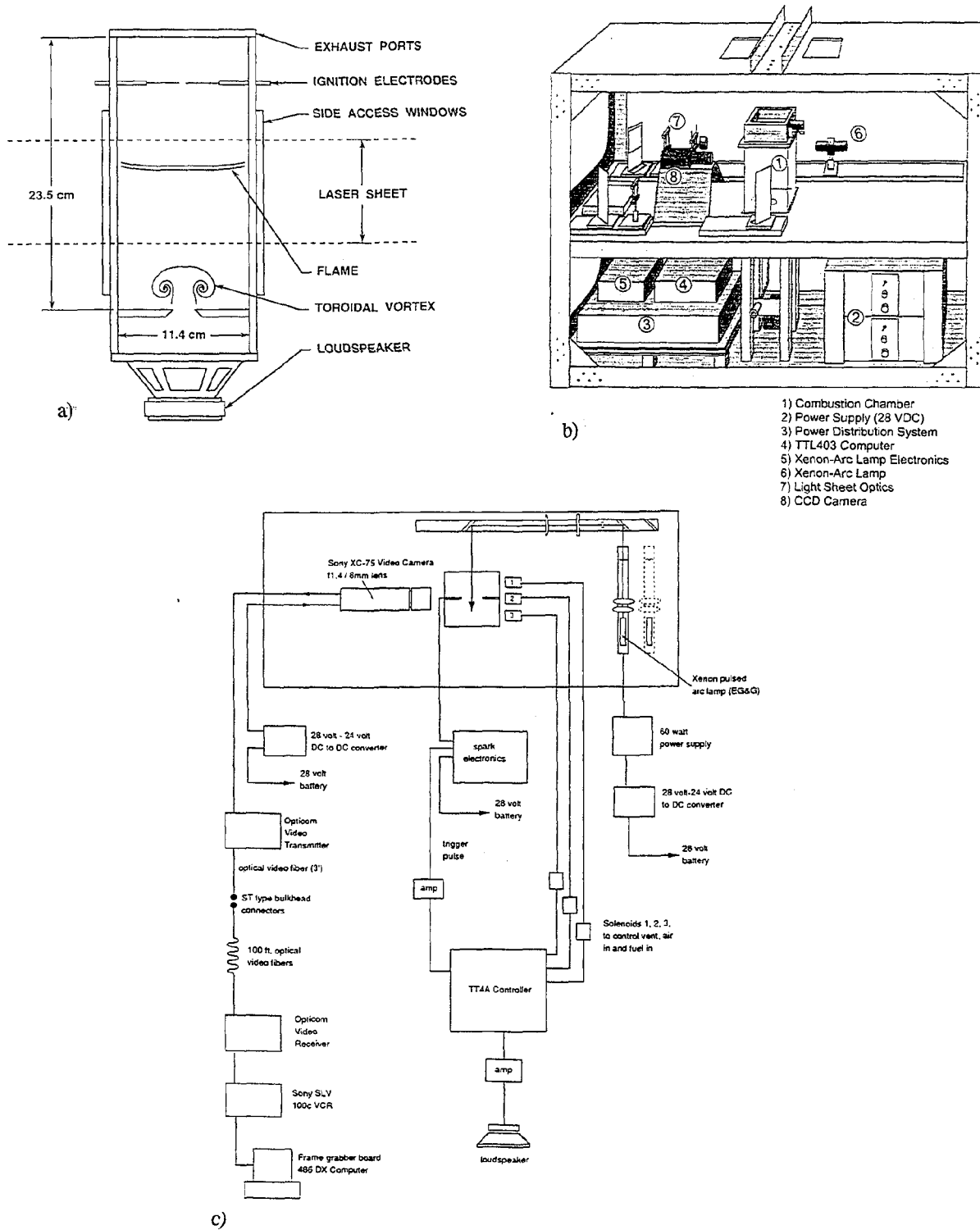
Figure 1: Schematic of the Microgravity Flame-Vortex Interaction Experiment.(a) Combustion Chamber; (b) Drop Rig used at NASA Lewis 2.2 Second Drop Tower; (c) Control & Power systems schematic.
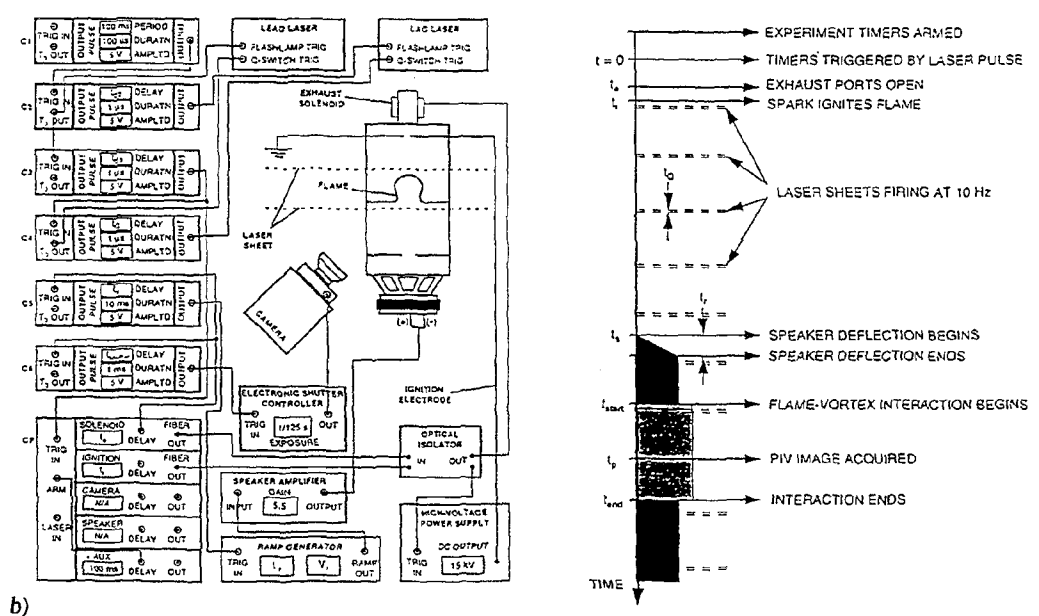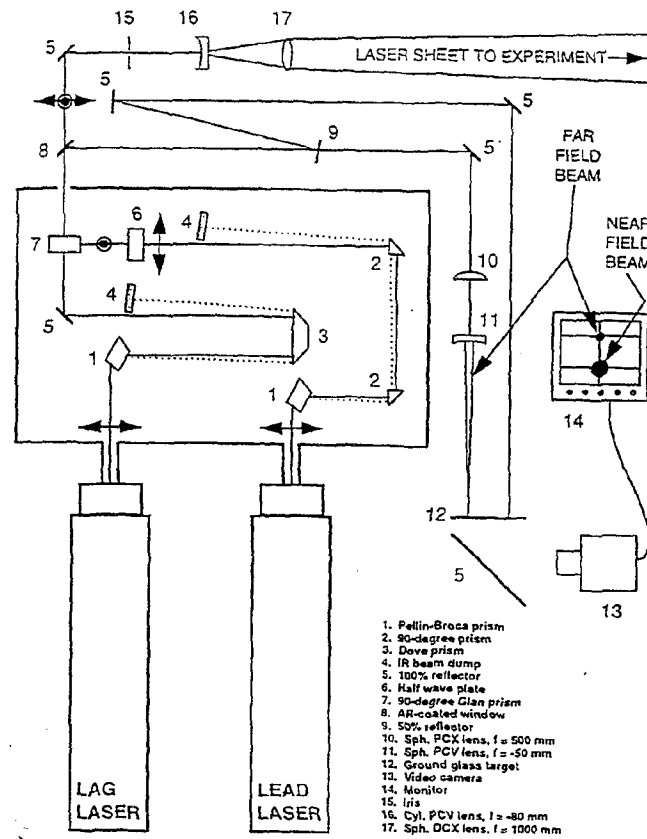
1. Pellin-Broca prism
2. 90-degree prism
3. Dove prism
4. IR beam dump
5. 100% reflector
6. Half wave plate
7. 90-degree Glan prism
8. AR-coated window
9. 50% reflector
10. Sph. PCX lens, f = 500 mm
11. Sph. PCV lens, f = -50 mm
12. Ground glass target
13. Video camera
14. Monitor
15. Iris
16. Cyl. PCV lens, f = -80 mm
17. Sph. DCX lens, f = 1000 mm

a)

b)

Figure 2: (a) Schematic of the PIV System for One-G Studies; (b) Control & Power systems schematic.
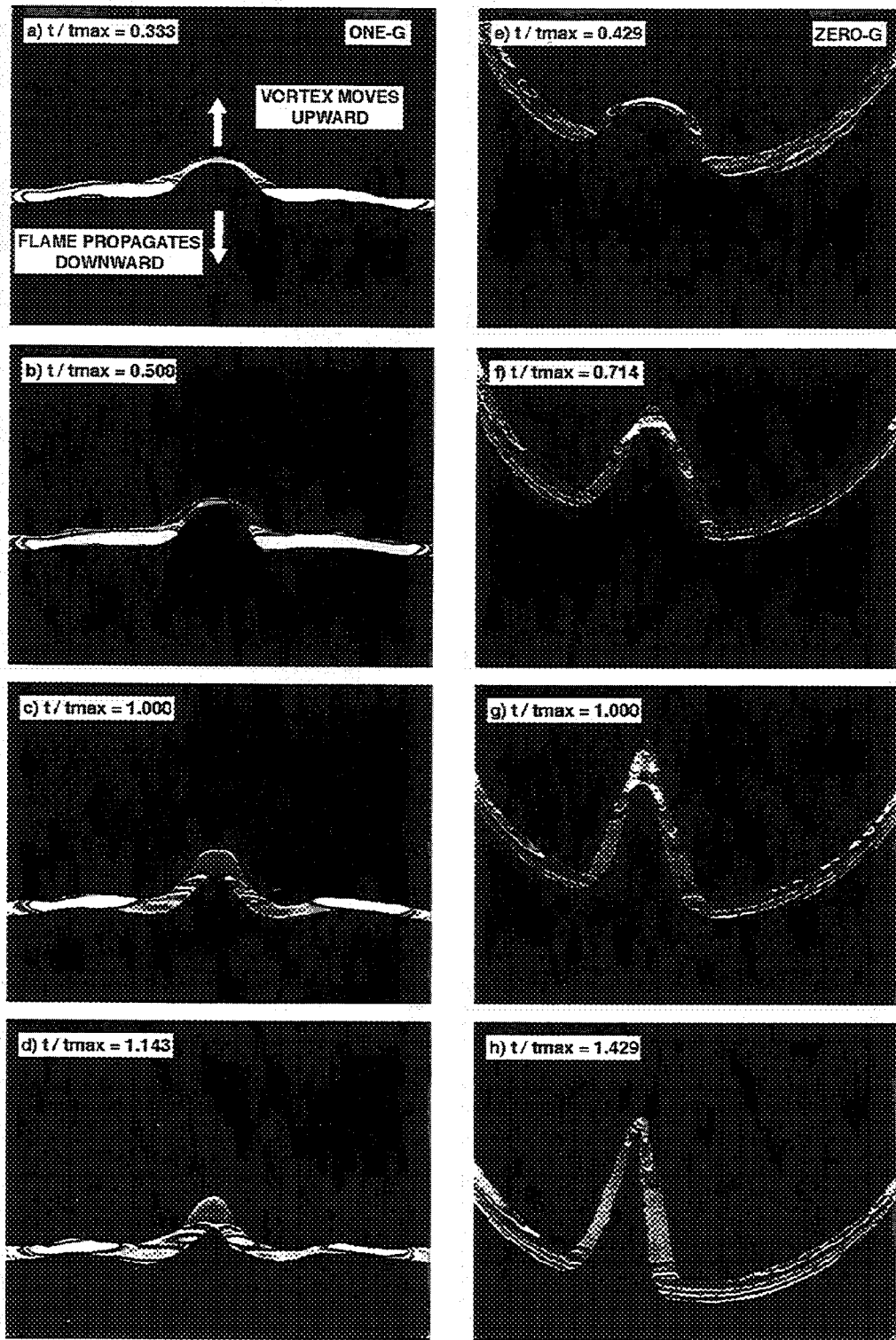
Figure 3: Increase In Flame Wrinkling Due To Microgravity For The Weak Vortex Interaction (Case A). Microgravity images appear on the right. Vortex moves upwards. tmax = time of maximum wrinkling = 100 ms (one-g), 167 ms (zero-g).
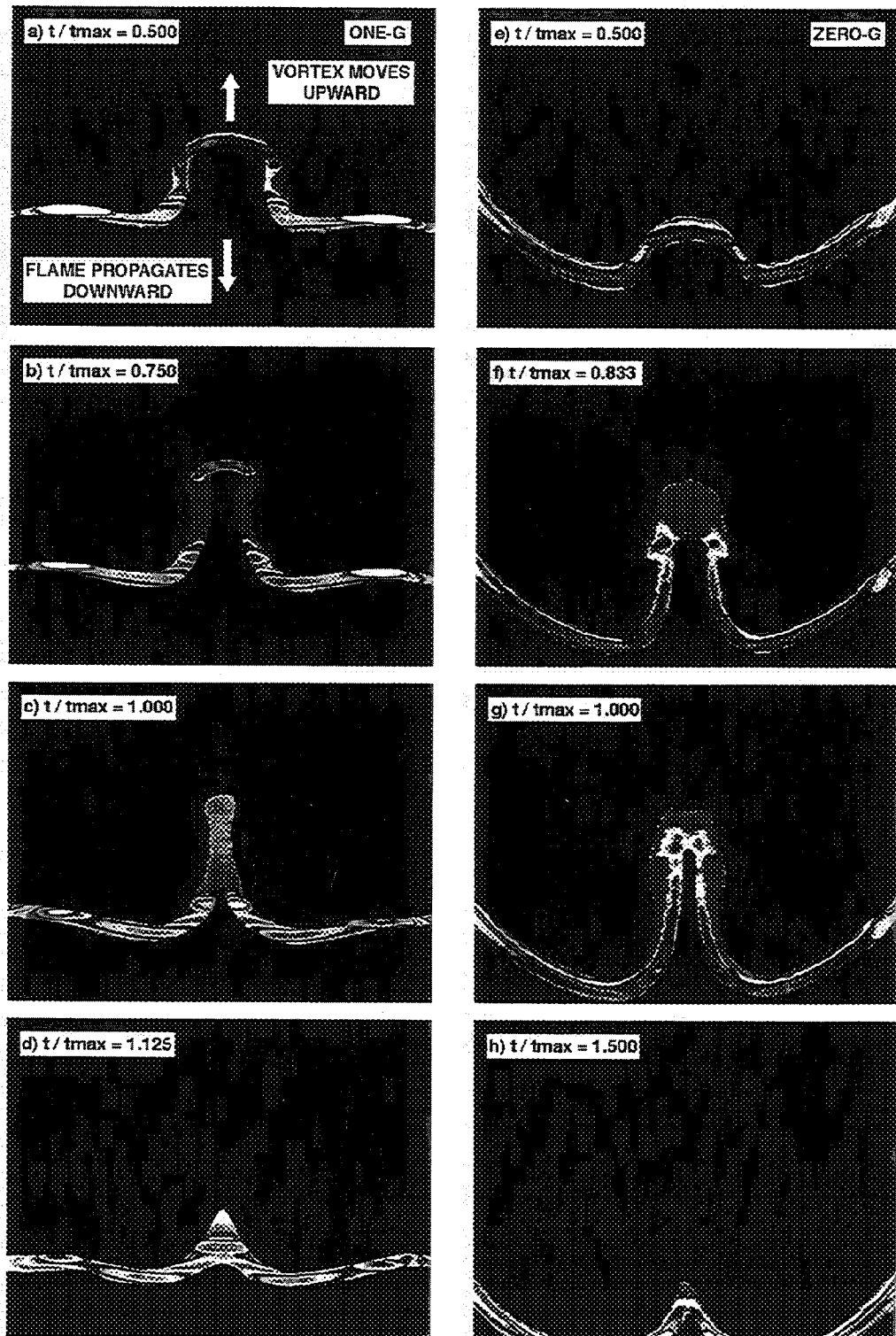
Figure 4: Increase In Flame Wrinkling Due To Microgravity For The Intermediate Strength Vortex Interaction (Case B). Microgravity images appear on the right. Vortex moves upwards. tmax = time of maximum wrinkling = 133 ms (one-g), 100 ms (zero-g).
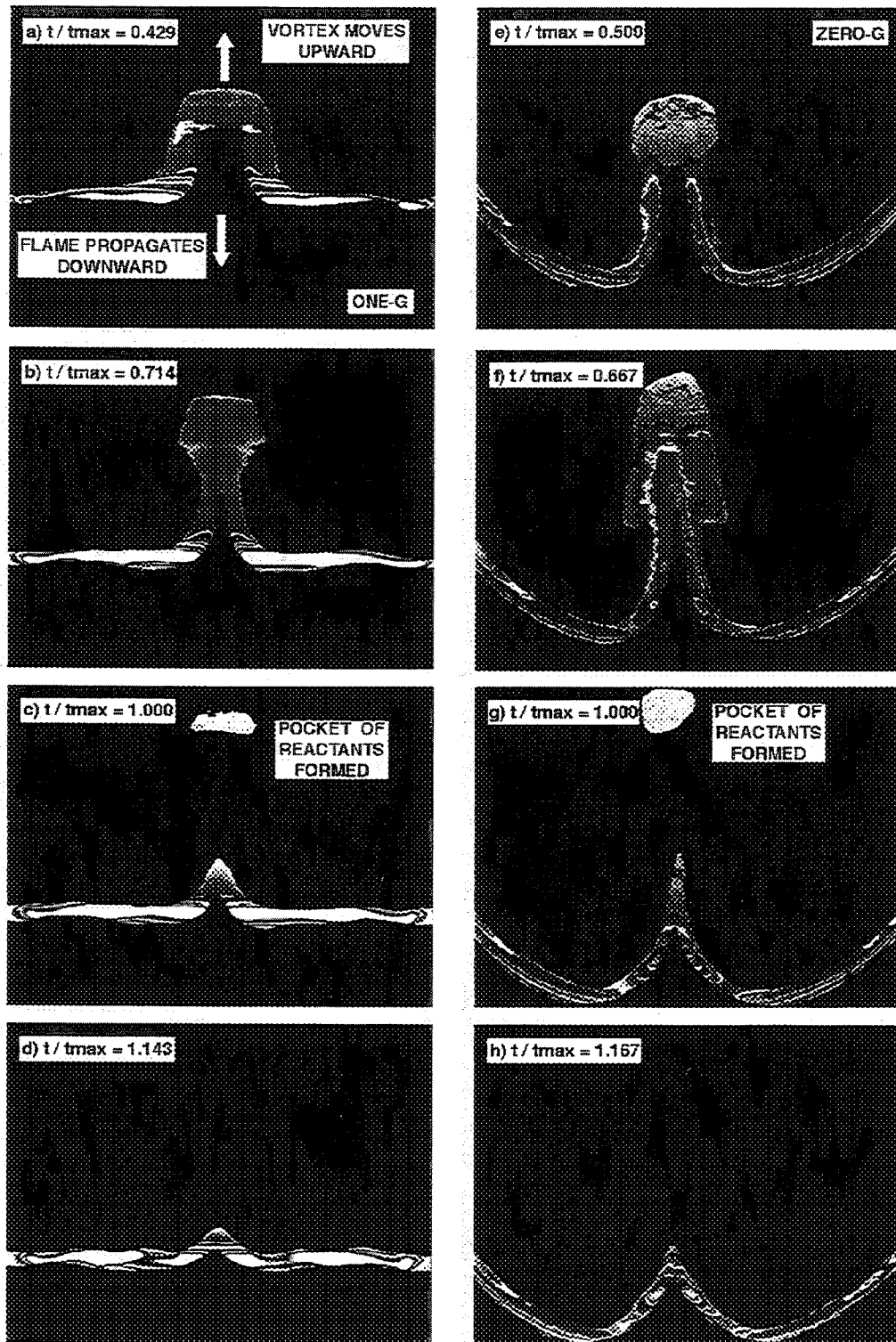
Figure 5: Increase In Flame Wrinkling Due To Microgravity For The Strong Vortex Interaction (Case C). Microgravity images appear on the right. Vortex moves upwards. tmax = time of maximum wrinkling = 117 ms (one-g), 100 ms (zero-g).
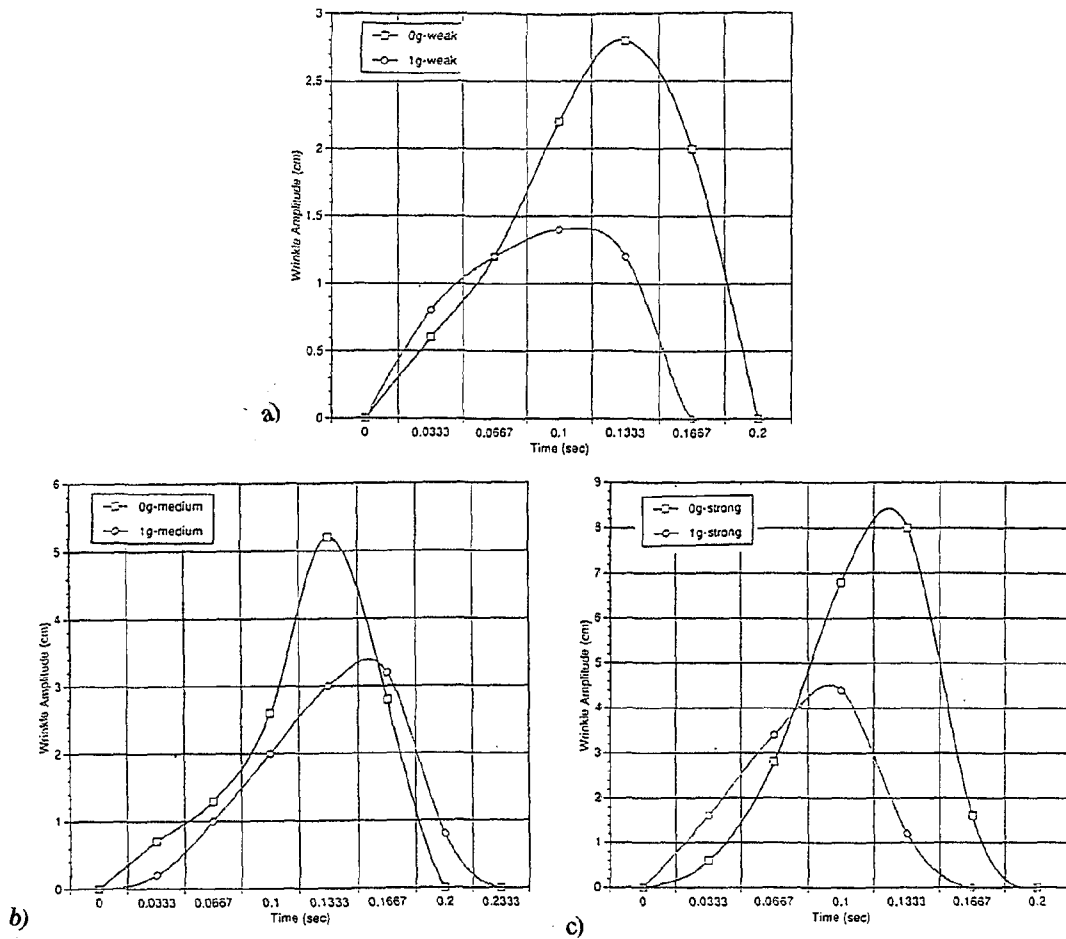
Figure 6: Measured Amplitudes of Flame Wrinkles Due to Vortex Interaction in Microgravity. (One-G shown for comparison.) (a) "Weak Vortex" case; (b) "Intermediate Vortex" case; (c) "Strong Vortex" case.
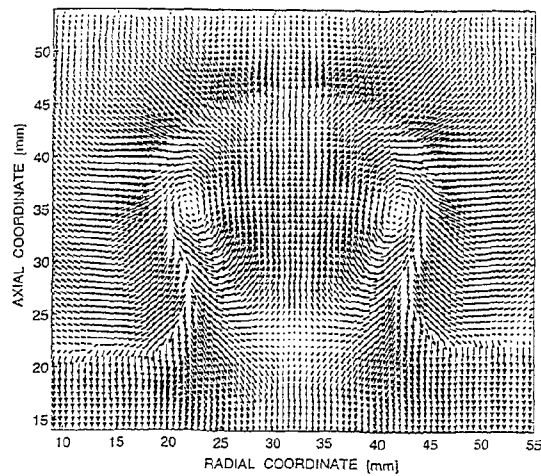
Figure 7: A Typical Velocity Field Image Measured Using PIV. (6000 vectors shown.)
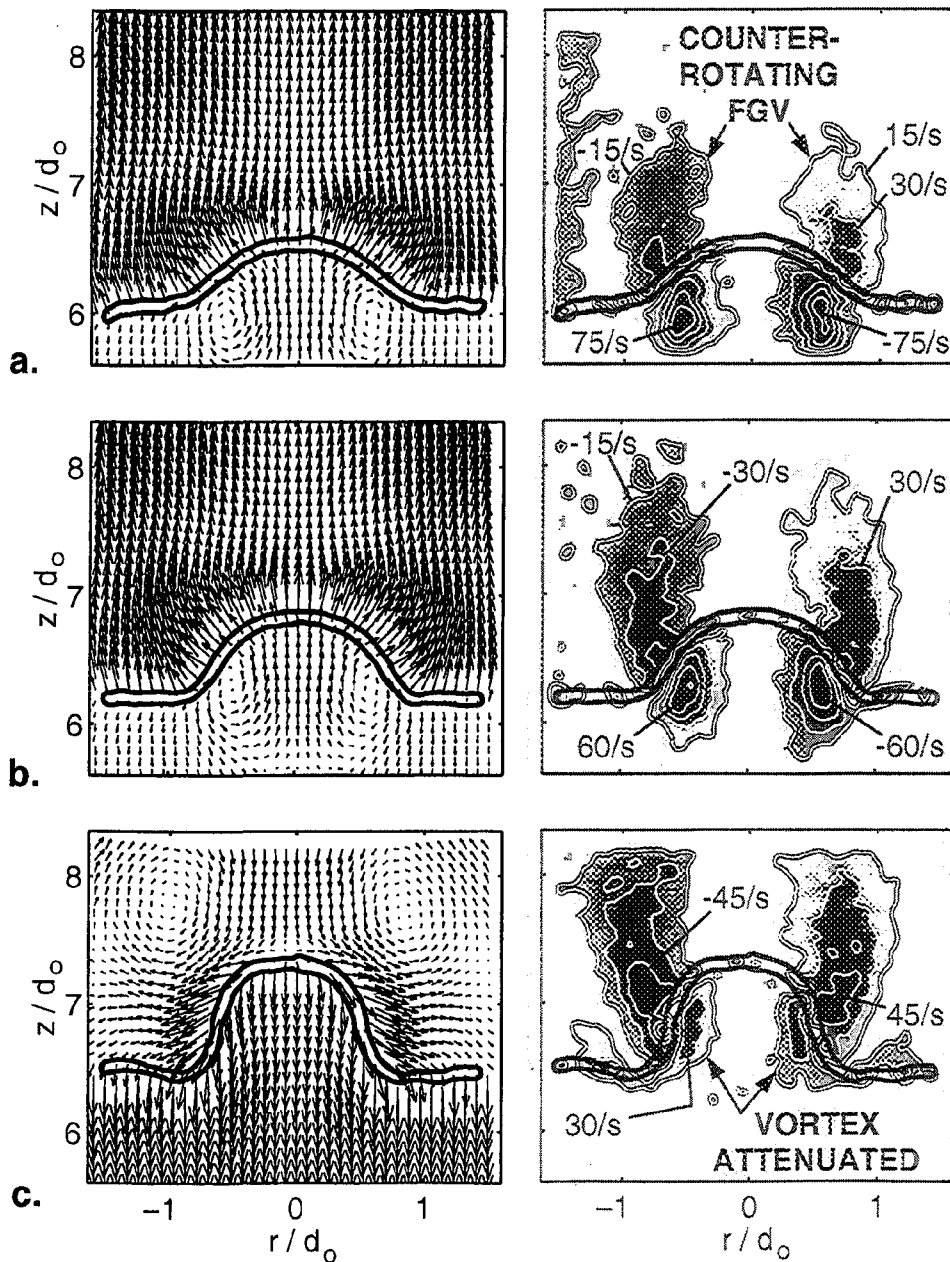
Figure 8: Measured Velocity and Vorticity Field Pairs for the case A Interaction (weakest vortex, $U_\theta/S_L = 1.4$) Incident vortex is completely eliminated by the flame, which generates vorticity similar in magnitude but opposite in sign to that of the incident vortex. The first two velocity images are in a reference frame that moves with the vortex; the rest move with the average velocity of the product gases to show that vorticity generated by the wrinkled flame induces a velocity field that tends to oppose flame wrinkling.
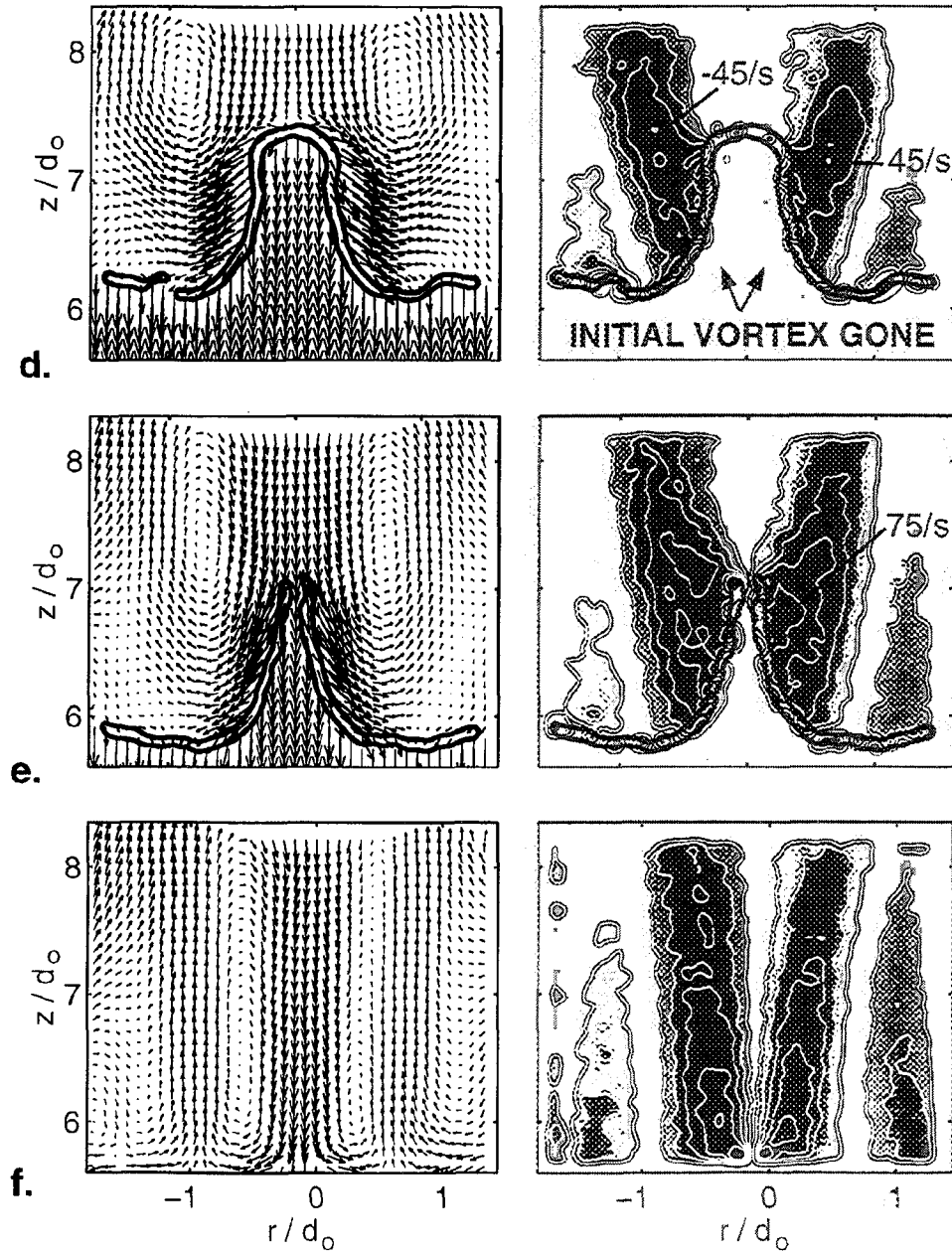
Figure 8 (cont'd): Measured Velocity and Vorticity Field Pairs for the case A Interaction. Rotational velocity of vortex alone is $U_\theta = 13$ cm/s; Da = 4.3. Regions of positive and negative vorticity are colored red and blue, respectively. Magnitudes of vorticity contours are 15, 30, 45, 60 s^{-1}. Times since the onset of wrinkling for Figs. (a) through (f) are 50, 75, 95, 130, 160, and 200 ms, respectively.
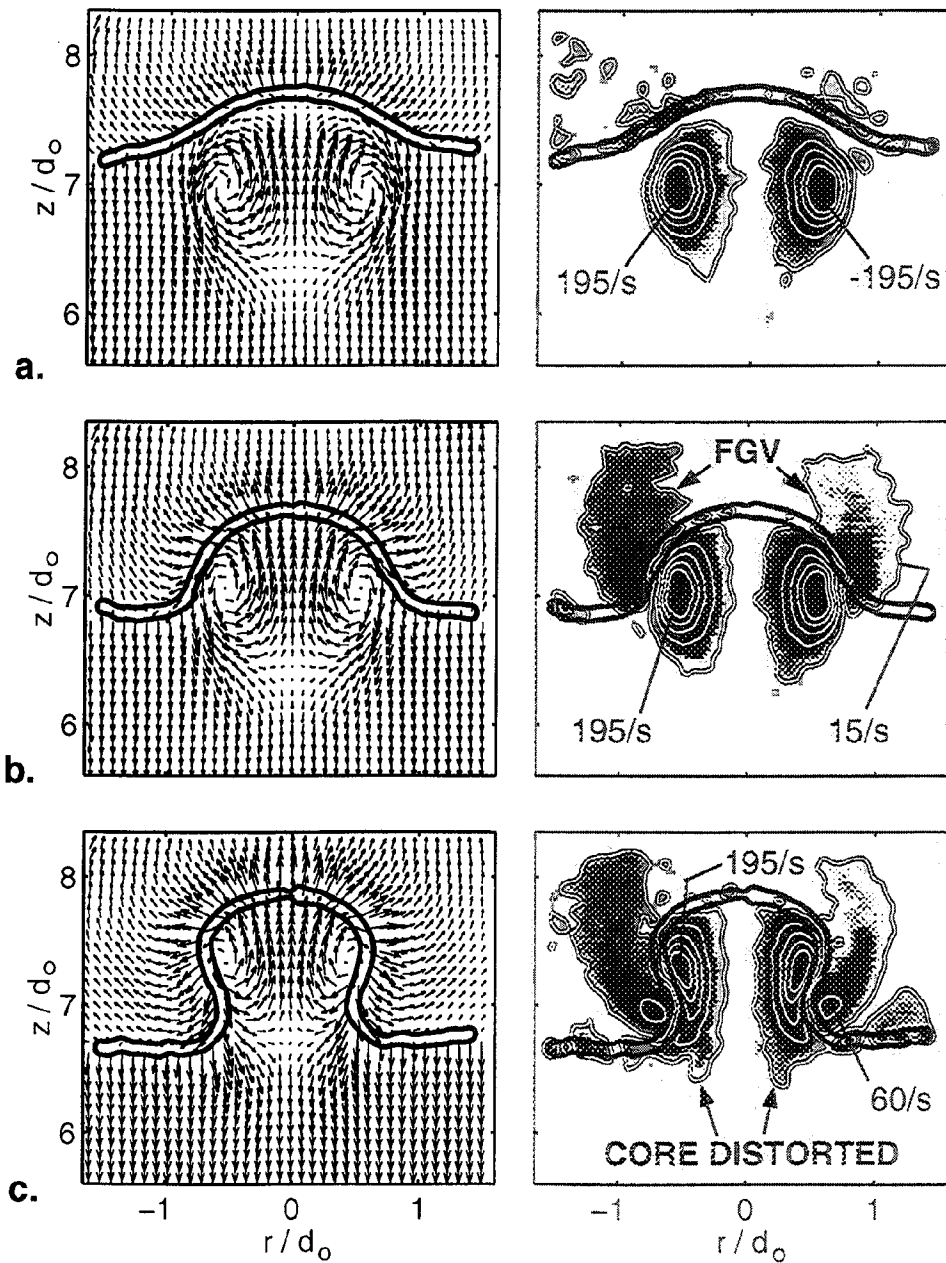
American Institute of Aeronautics and Astronautics

Figure 9: Measured Velocity and Vorticity Field Pairs for the case B Interaction (intermediate vortex, $U_\theta/S_L = 3.6$) Some of the initial circulation, though significantly attenuated by volume expansion and FGV, survives passage of the flame. Velocity vectors are in the vortex frame of reference.
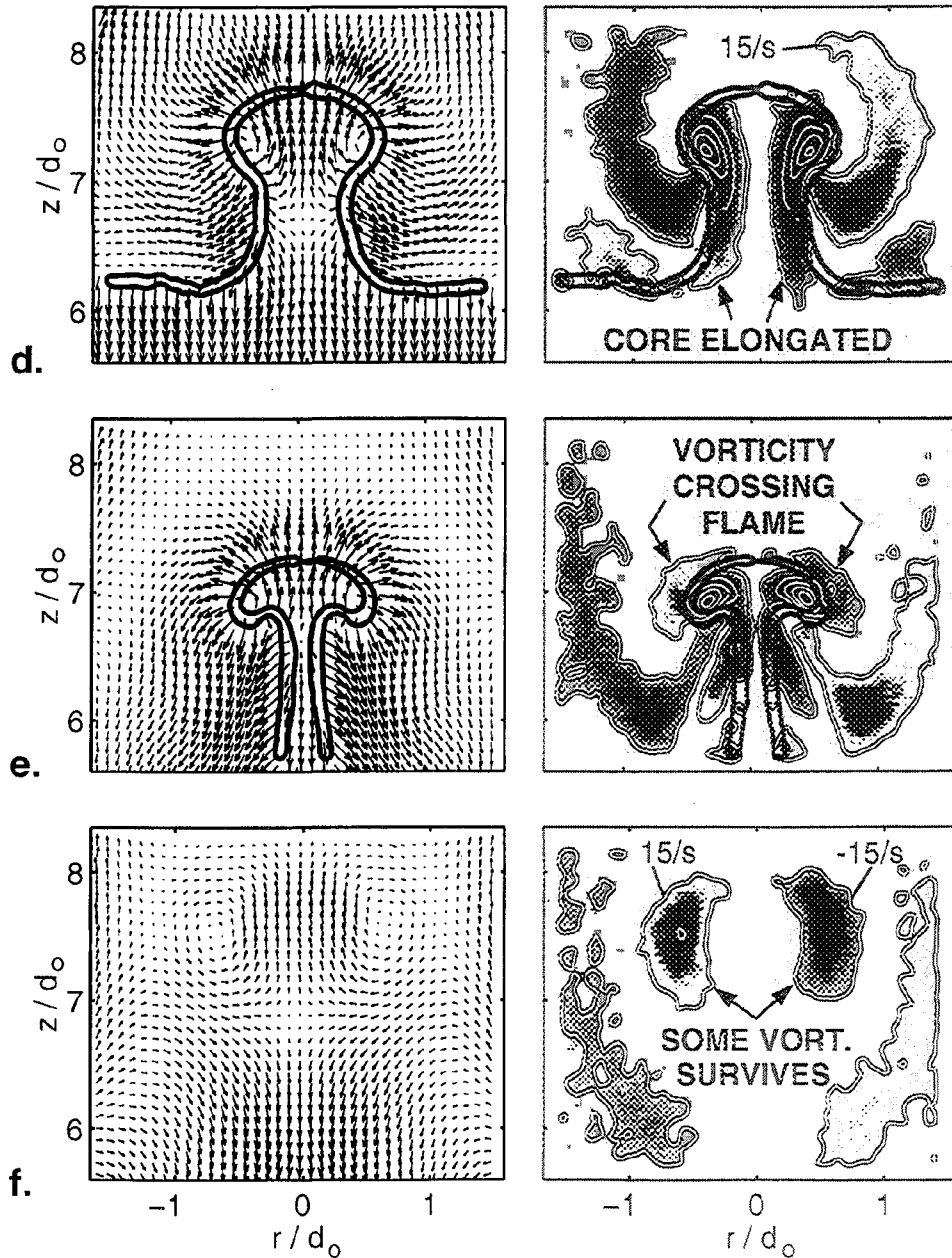
Figure 9 (cont'd): Measured Velocity and Vorticity Field Pairs for the case B Interaction. Rotational velocity of vortex alone is $U_\theta = 34$ cm/s; Da = 1.4. Regions of positive and negative vorticity are colored red and blue, respectively. Magnitudes of vorticity contours are 15, 60, 105, 150, and 195 s^{-1}. Times since the onset of wrinkling for Figs. (a) through (f) are 25, 40, 55, 63, 78, and 105 ms, respectively.
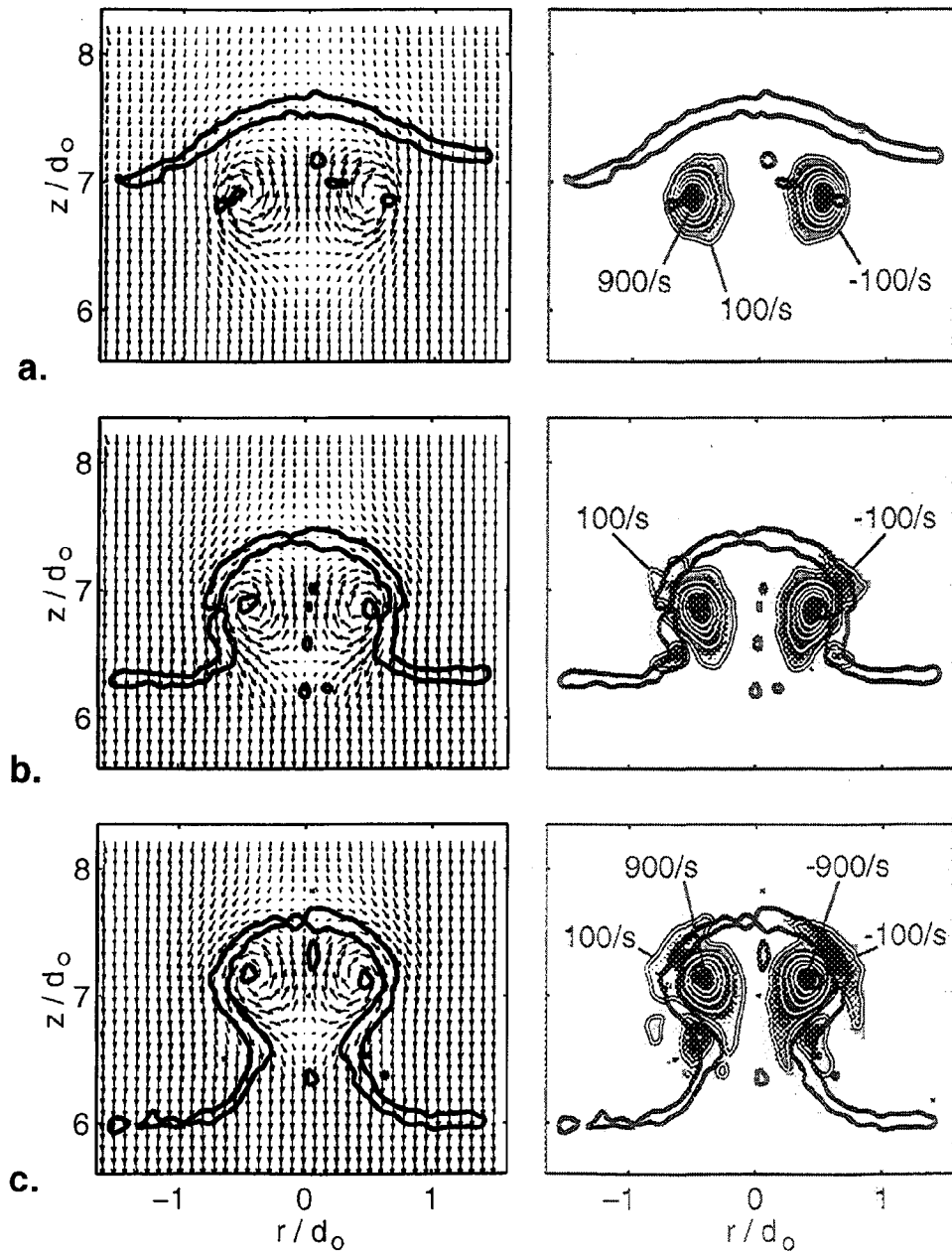
Figure 10: Measured Velocity and Vorticity Field Pairs for the case C Interaction (strong vortex, U_θ/S_L= 10) Incident vortex provides sufficient stretch rate and residence time to locally extinguish the flame. Velocity vectors are in the vortex frame of reference.
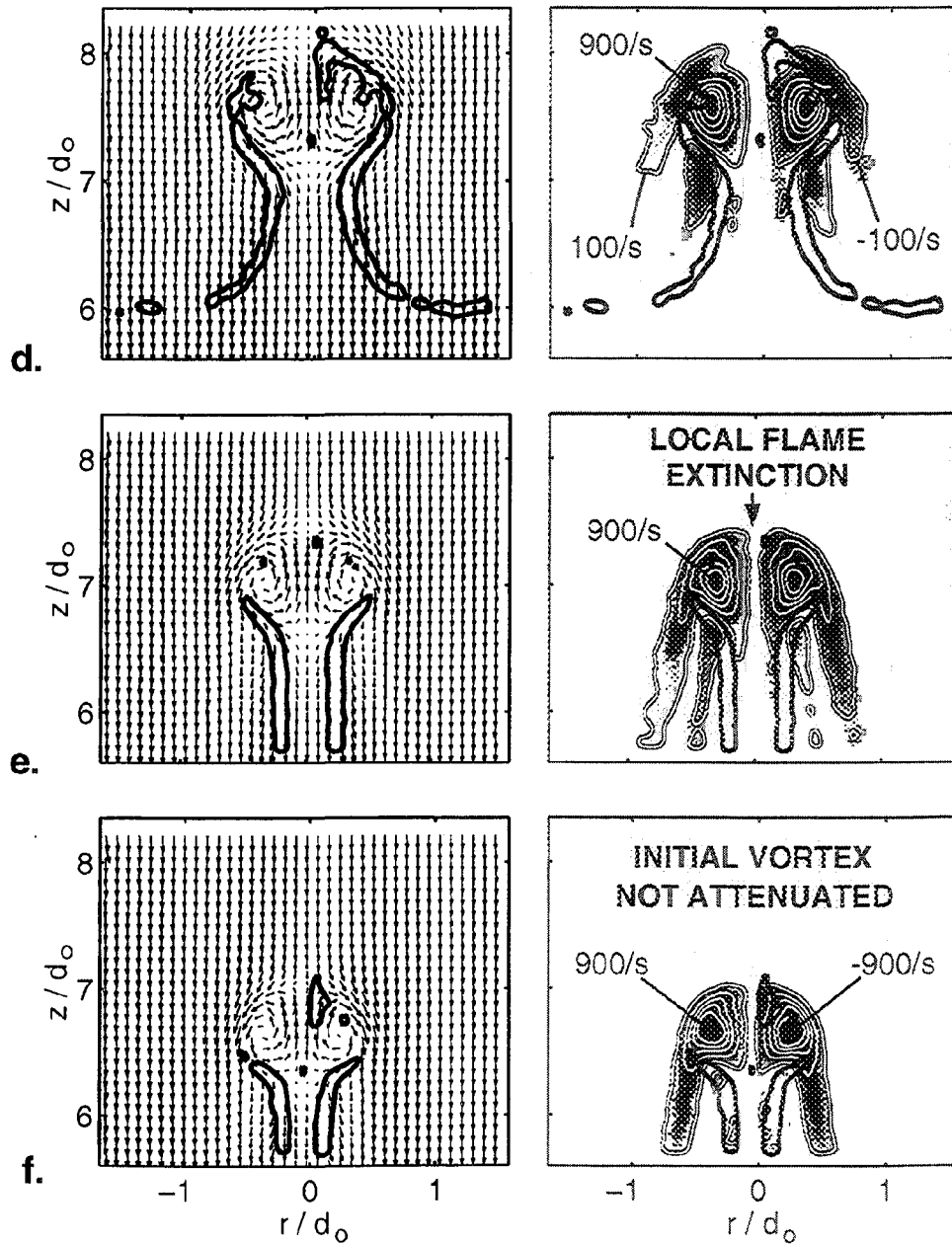
Figure 10 (cont'd): Measured Velocity and Vorticity Field Pairs for the case C Interaction. Rotational velocity of vortex alone is U_θ = 98 cm/s; Da = 0.37. Regions of positive and negative vorticity are colored red and blue, respectively. Magnitudes of vorticity contours are 100, 300, 500, 700, and 900 s^{-1}. Times since the onset of wrinkling for Figs. (a) through (f) are 8, 13, 16, 18, 21, and 25 ms, respectively.
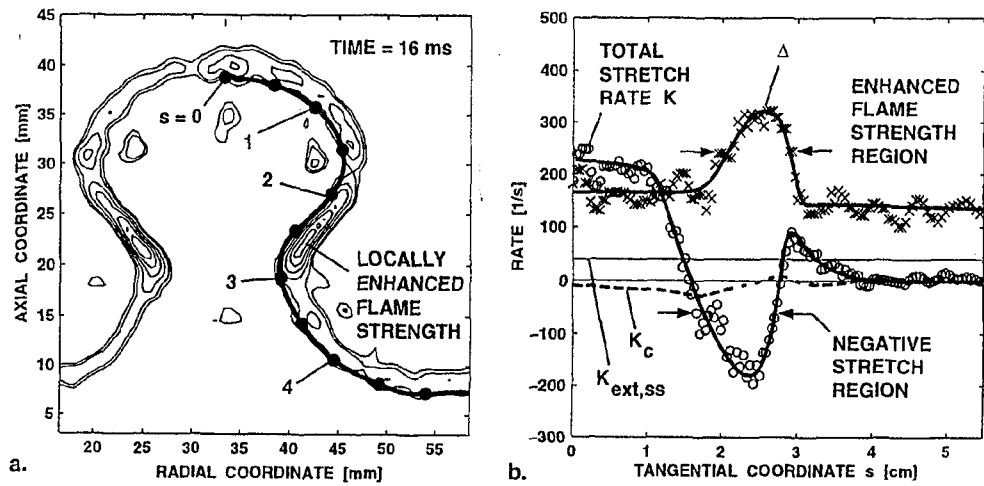
Figure 11: Dilatation Rate, Stretch, and Flame Strength Distributions at 16 ms after the Onset of Wrinkling. (a) Contours of dilatation rate, showing locally-enhanced flame strength in the neck region of the flame. (b) Measured distributions of local stretch rate K and flame strength Δ along the flame. Enhanced flame strength evident in (a) corresponds to a region of compressional flame stretch. Stretch in the centerline is extensional and exceeds $K_{ext,ss}$ by a factor of approximately 6, yet centerline flame strength is approximately equal to that of the unstretched, flat flame (s=5cm). The curvature component of the stretch rate, K_c, is shown by the dashed line and seen to be small.
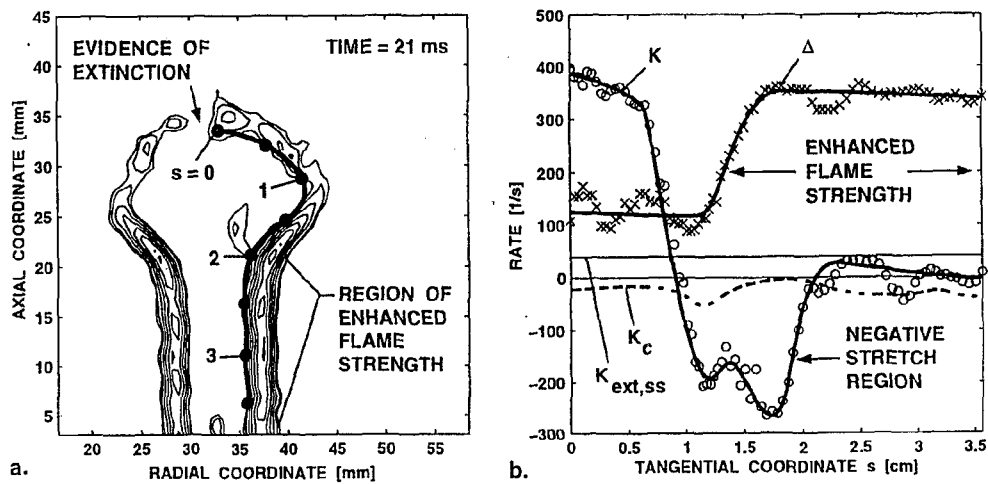

Figure 12: Dilatation Rate, Stretch Rate, and Flame Strength Distributions at 21ms.after the Onset of Wrinkling. (a) Dilatation rate contours showing evidence of local extinction near the leading edge of the interaction and also enhanced flame strength in the neck region of the flame. (b) Measured distributions of local stretch rate K and flame strength Δ along the flame. Stretch in the centerline is extensional and exceeds $K_{ext,ss}$ by a factor of approximately 10. The curvature component of the stretch rate, K_c, is seen to be growing more negative in the neck region of the flame.
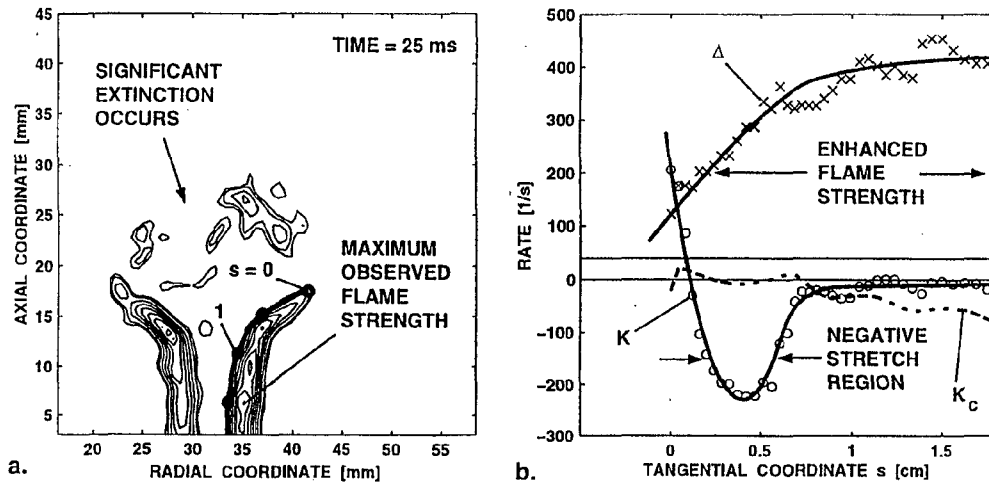
American Institute of Aeronautics and Astronautics

Figure 13: Dilatation Rate, Stretch Rate, and Flame Strength Distributions at 25ms.after the Onset of Wrinkling. (a) Dilatation rate contours showing evidence of significant local extinction at the leading edge of the interaction. Enhanced flame strength is again seen in the neck region of the flame. (b) Measured distributions of local stretch rate K and flame strength Δ along the flame. Again, this shows flame strength increasing strongly through a region of negative flame strain, and the maximum observed flame strength is in the strongly curved neck region. Note that the s = 0 location does not correspond to the leading edge of the interaction as in previous figures, but rather marks the upper end of the non-extinguished flame.